Magnetic Resonance Imaging 64 (2019) 13–20

Contents lists available at ScienceDirect

Magnetic Resonance Imaging

journal homepage: www.elsevier.com/locate/mri

Original contribution

Synthesizing T1 weighted MPRAGE image from multi echo GRE images via deep neural network

Kanghyun Ryu[a], Na-Young Shin[b], Dong-Hyun Kim[a,*], Yoonho Nam[b,**]

[a] Department of Electrical and Electronic Engineering, Yonsei University, Seodaemun-gu, Seoul 120-749, Republic of Korea
[b] Department of Radiology, Seoul St. Mary's Hospital, College of Medicine, The Catholic University of Korea, Seoul 065-591, Republic of Korea

ARTICLE INFO

Keywords:
MPRAGE
Multi echo GRE
Convolutional neural network
U-Net
QSM

ABSTRACT

For quantitative neuroimaging studies using multi-echo gradient echo (mGRE) images, additional T_1-weighted magnetization prepared rapid gradient echo (MPRAGE) images are often acquired to supplement the insufficient morphometric information of mGRE for tissue segmentation which require lengthened scan time and additional processing such as image registration. This study investigated the feasibility of generating synthetic MPRAGE images from mGRE images using a deep convolutional neural network. Tissue segmentation results derived from the synthetic MPRAGE showed good agreement with those from actual MPRAGE (DSC = 0.882 ± 0.017). There was no statistically significant difference between the mean susceptibility values obtained with the regions of interest from synthetic and actual MPRAGEs and high correlation between the two measurements.

1. Introduction

MR-based brain morphometry studies typically accompany the acquisition of high-resolution T_1-weighted magnetization prepared rapid gradient echo (MPRAGE) sequence which provides excellent gray/white matter contrast [1]. The morphometric information obtained from MPRAGE is also useful for quantitative analysis of functional or parametric mapping studies based on other contrast images which have low spatial resolution or insufficient tissue contrast.

Recently, T_2^* or quantitative susceptibility mapping (QSM) studies [2–5] based on multi-echo GRE images have been widely used for these studies because of its high sensitivity to materials with magnetic susceptibility variations such as iron or myelin. For these studies, the additional MPRAGE images are valuable when performing region-based group analysis or longitudinal analysis [6–8] but require additional scan time. Recent fast imaging techniques can relieve the burden of additional acquisition time for MPRAGE [9], however, they are not yet generally available. Moreover, in retrospective studies, there are many cases of mGREs acquired without an additional MPRAGE acquisition. The ability to synthesize MPRAGE images using acquired mGRE images has potential values in reducing scan time and improving analysis tasks which need registration and segmentation.

Synthetically generating medical images using deep learning have shown notable performance in various studies. For example, CT image reconstruction with an MR image without an actual CT scan [10–12], 7T MR image reconstruction from 3 T MR images [13] and MR image synthesis from different scan parameters [14]. These deep learning methods learn intensity transformation between two images by feeding large datasets and use the learned information to reconstruct synthetic images. They are an extended form of intensity-transform-based synthesis methods, which learn sparse linear representations between the two images [15,16]. Using multiple layers of neural network, deep learning can efficiently learn nonlinear and complex transformation. It has also been demonstrated to yield higher synthesis quality compared to non-network-based approaches [11,13]. Considering the current performance of the deep neural networks in these applications, the approach may be applicable for learning the transformation between mGRE images and MPRAGE images.

Here, we have developed and applied a deep-learning based method to synthetically construct MPRAGE image from single scan mGRE images. To demonstrate the utility of our synthetic MPRAGE, we compared the automatic segmentation results from the synthetic MPRAGE with those from the actual MPRAGE. In addition, using the two tissue segmentation results, the average susceptibility values in the deep gray matter regions calculated from mGRE images were compared. As a preliminary attempt to further explore the clinical applicability of the method, we tested our method on two clinical images containing pathologies which were not seen in the training set.

* Correspondence to: D.-H. Kim, Department of Electrical and Electronic Engineering, Yonsei University, Seoul, Republic of Korea.
** Correspondence to: Y. Nam, Department of Radiology, Seoul St. Mary's Hospital, College of Medicine, The Catholic University of Korea, Seoul, Republic of Korea.
E-mail addresses: donghyunkim@yonsei.ac.kr (D.-H. Kim), yhnam83@gmail.com (Y. Nam).

https://doi.org/10.1016/j.mri.2019.04.002
Received 20 December 2018; Received in revised form 13 March 2019; Accepted 2 April 2019

2. Methods and materials

2.1. Subjects

A total of 28 healthy volunteers (22 female and 6 male, age: 25–39 years, median age: 28 years) were recruited with written consent. Of the total dataset from the volunteers, the network was trained from the images from 20 subjects and was evaluated in 8 subjects excluded in the training set. To investigate how the trained network responded to untrained imaging features, additional MR images of 8 subjects (age: 27–81 years, median age: 40) were retrospectively collected from our hospital database. The study was approved by the local Institutional Review Board.

2.2. Imaging procedure

The study was performed on a Phillips Ingenia 3T MRI scanner (Philips Healthcare, Best, the Netherland) with a 32 channel receive coil. The routine protocols for multi-echo 3D GRE and MPRAGE at our institution were conducted for all volunteers. Scan parameters for the mGRE were as follows: voxel size = $0.8 \times 0.8 \times 2\,mm^3$, 72 axial slices, TR = 30 ms, TE = 7.20, 13.6, 20.0, 26.4 ms for 4 echoes, flip angle = 17°, parallel imaging acceleration factor = 2, scan time = 3 min 16 s. Scan parameters for MPRAGE were as follows: voxel size = $1 \times 1 \times 1\,mm^3$, 176 sagittal slices, TR = 6.8 ms TE = 1.5 ms, TI = 1100 ms, flip angle = 7°, parallel imaging acceleration factor = 2, scan time = 5 min 21 s.

2.3. Data pre- and post-processing

To match the resolution and field of view of the image and correct for motion-induced displacements between the two sequences, mGRE images were rigidly registered to 1 mm isotropic MPRAGE images using the FLIRT toolbox [17] inside FSL (Oxford, UK). After registration, the intensities of each pixel were rescaled linearly to be within the range of 0 to 1, by dividing by the maximum pixel intensity value of each image. This step was essential in reducing the variations of the input data and the label data for effective training.

Each 3D data was then split by multiple patches with a size of $64 \times 64 \times 64$ to fit in the memory of the graphical processing unit (GPU, NVIDIA GeForce GTX – 1080 TI GPU with 11GB GPU memory). During this process, patch overlapping was performed to increase the number of patches and reduce the patch-induced blocky artifacts of the combined results. This is often referred to as the overlap-tile strategy when training large size images [18]. The overlapping region was set at 8 voxels with neighboring patches, which was chosen to be sufficient for removing the discontinuity. During testing, the patches were combined to a single image by averaging the overlapping regions.

2.4. Network implementation and training details

For the network, we adopted the standard U-Net architecture which has previously demonstrated successful results in various biomedical imaging applications including pixel-wise segmentation [18], synthetic image generation [19], and artifact removal [20]. Instead of using the original version of the U-Net architecture which was developed for 2D image data, we used the 3D version of U-Net [21] to learn the 3D context of the three-dimensionally encoded MR data.

The overall detail of the network architecture is shown in Fig. 1. Patches of four mGRE images were concatenated and put into the input of the network. The encoder network was composed of $3 \times 3 \times 3$ kernel convolutional layers and nonlinear activations, rectified linear unit (ReLU). Prior to each convolutional layer, zero-padding was applied so that the output size remained the same as the input size. After performing three convolutional layers and nonlinear activation layer, a max-pooling operation layer with a $2 \times 2 \times 2$ window and stride of 2 was applied. The number of filters for each convolutional layer is shown in Fig. 1. For the decoder network, the network structure was symmetric to the encoder network except for the max pooling operation which was replaced with the deconvolution operation with a kernel size of $5 \times 5 \times 5$ and strides of $2 \times 2 \times 2$. To copy over the intermediate outputs of the encoding parts to the decoding parts, extra connections (skip connections) were made. These skip connections pass intermediate features of the encoding part to the decoder part which are known to be effective for producing finer output [18].

The full network can be considered as representing an end-to-end mapping function that transforms the input mGRE images to their corresponding MPRAGE image. The learning was achieved by minimizing a loss between the predicted MPRAGE image (synthetic) and actual MPRAGE image (label). We used the combined mean absolute error (MAE) and total variation error (TV) as the loss function with a ratio of 1:0.1. Specifically, for a single image the loss was designed as:

$$\text{Loss} = \sum_{i,j} |Y_{i,j} - \hat{Y}_{i,j}| + 0.1 \bullet \sum_{i,j=1}^{n} ||Y_{i,j} - Y_{i-1,j}| - |\hat{Y}_{i,j} - \hat{Y}_{i-1,j}|| + ||Y_{i,j-1} - Y_{i,j}| - |\hat{Y}_{i,j-1} - \hat{Y}_{i,j}|| \quad (1)$$

where Y is the actual MPRAGE image and $\hat{Y}$ is the predicted MPRAGE image. Adding the total variation error penalizes image gradient differences, that is neighboring pixel intensity differences. It has been effective in preserving sharp edges of the synthesized images, especially in recovering delicate structures [22–24]. The ratio of the two loss functions were optimized by varying the weighting from 1:0.01 to 1:1, in which ratio of 1:0.1 showed the minimum loss. The network was implemented using Python-based Tensorflow library (version 1.2.1). The whole network parameters needed for training were 813,009. The network was trained by mini-batch training with a batch size of 20 using the Adam optimizer with a learning rate of 10^{-4}. During training, we used data augmentation by flipping in three dimensions and scaling by a random value in the range of [0.9 1.1] at every iteration and two subjects' data were used as validation set for network parameter tuning. The number of epochs was empirically determined by tracking the losses of the training and validation sets (400 in this study). The total learning took about 50 h of computation time for 400 epochs using the single NVIDIA GeForce GTX 1080 TI GPU.

2.5. Evaluation

In addition to visual evaluation, quantitative analysis was performed to evaluate the reconstruction performance of the synthetic images. To evaluate the image similarity between the synthetic MPRAGE and the actual MPRAGE, NRMSE (normalized root mean squared error) and SSIM (structural similarity metric) were calculated [25]. Because MPRAGE images are inherently not quantitative, the functionality of the synthetic results was also evaluated to determine whether the synthetic MPRAGE might have the ability to provide accurate information as compared to the actual MPRAGE. Since MPRAGE are widely used for tissue segmentation, the accuracy was determined to be the functionality metric for comparison. For this purpose, the following quantitative evaluation methods were performed.

First, both the synthetic and conventional MPRAGE images were fully automatically segmented using the FreeSurfer software [26] without any manual intervention. For the comparison metric, the dice similarity coefficient (DSC) was used [27]. The DSC measures the spatial overlap between the segmentation result and ground truth, having larger values for higher accuracy. It is defined as:

$$\text{DSC}(G, S) = \frac{2|G \cap S|}{|G| + |S|}, \quad (2)$$

where S is the binary segmentation result of the synthetic MPRAGE image and G is the segmentation result of the actual MPRAGE. For seven representative regions (cortex, cerebral white matter, putamen,

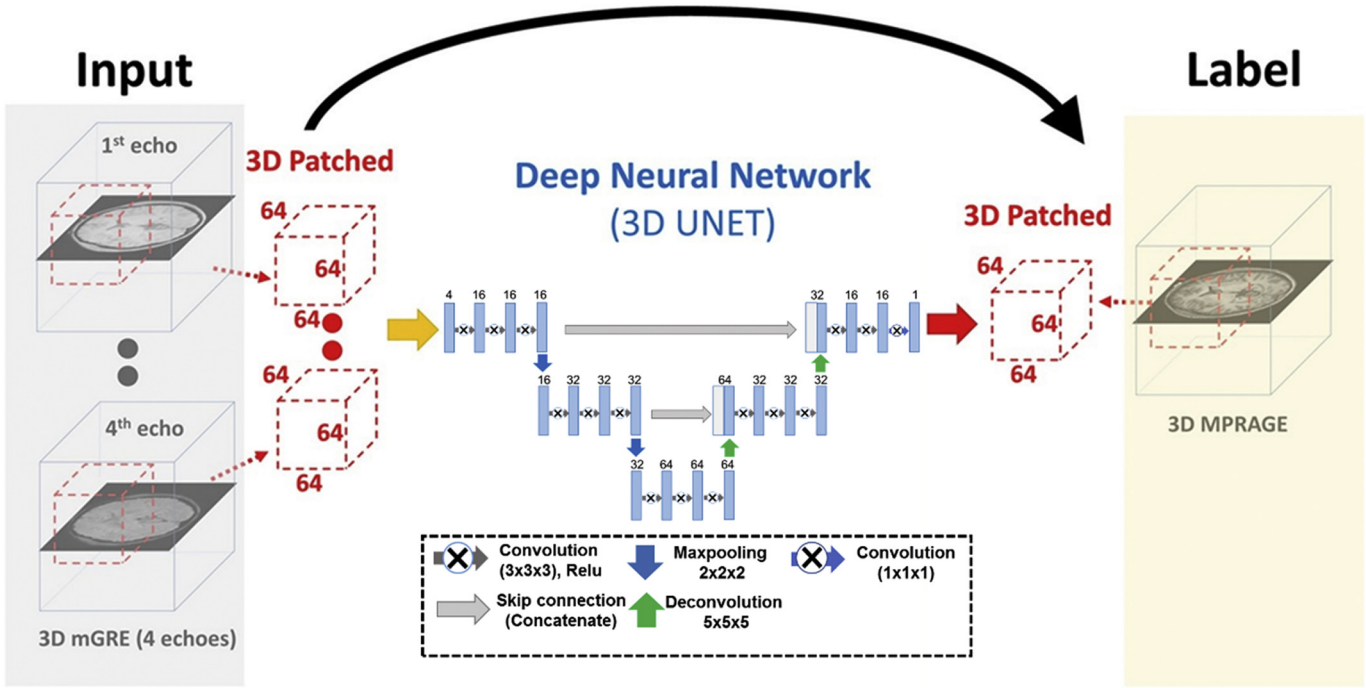

Fig. 1. The neural network architecture for synthesizing MPRAGE from mGRE. The whole process includes 3D patching and deep neural network (3D U-NET). The input images were the mGRE images and the label images were the actual MPRAGE images. Each blue box corresponds to a multi-channel feature map. The number of channels is denoted on top of the box. White boxes represent copied feature maps. (For interpretation of the references to colour in this figure legend, the reader is referred to the web version of this article.)

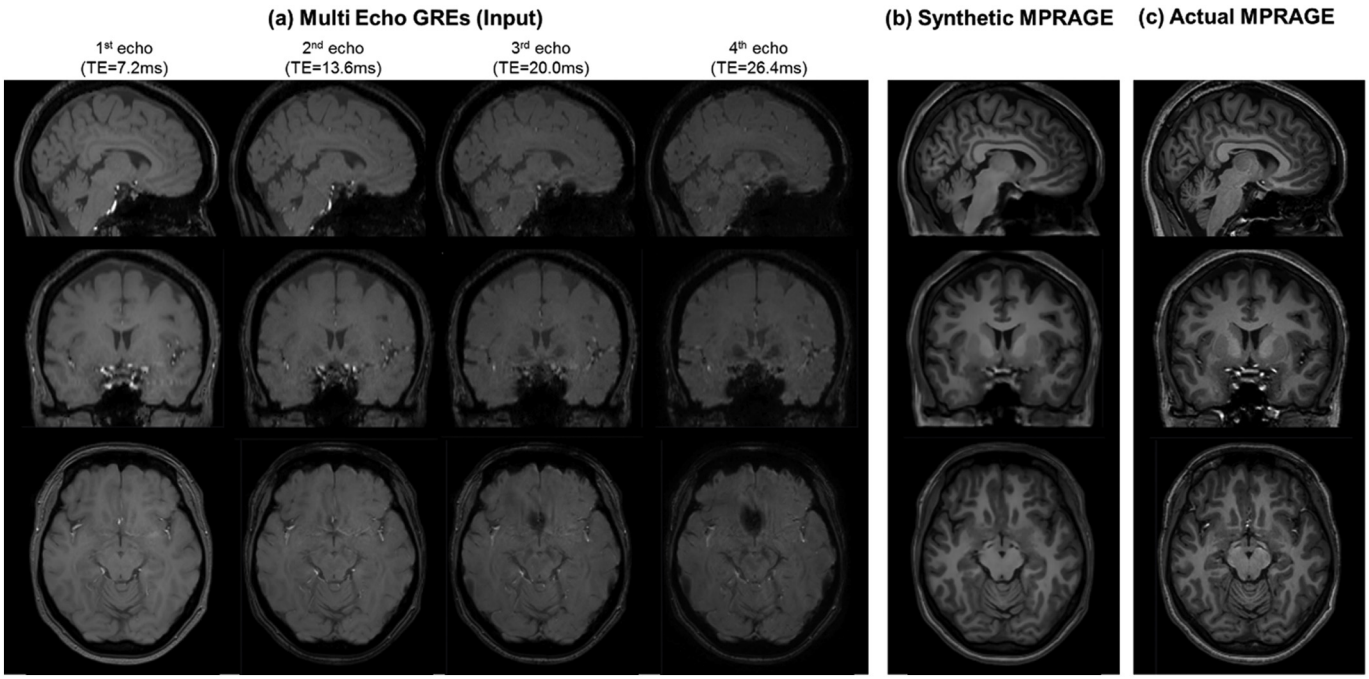

Fig. 2. Example images of synthetic MPRAGE and actual MPRAGE in three orthogonal views: sagittal (first row), coronal (second row), axial (third row). (a) mGRE magnitude images, (b) Synthetic MPRAGE images and (c) actual MPRAGE images.

pallidum, thalamus, caudate and hippocampus), the mean and standard deviation values of DSC were calculated from the automatically segmented results. In the procedure, the left and right hemispheres were considered separately. Therefore, the analysis was performed on 16 hemispheres in total.

In addition, using the segmentation results, a region-based quantitative analysis was performed following QSM reconstruction from the mGRE. QSM was reconstructed from the mGRE phase images using the sophisticated harmonic artifact reduction for phase data (SHARP) method [28] and the improved sparse linear equation and least-squares (iLSQR) method [29]. The average susceptibility values of deep gray matter regions (putamen, pallidum, thalamus, caudate) were obtained using the segmentation results from the actual and the synthetic MPRAGEs. To determine the statistical significance of the differences, a

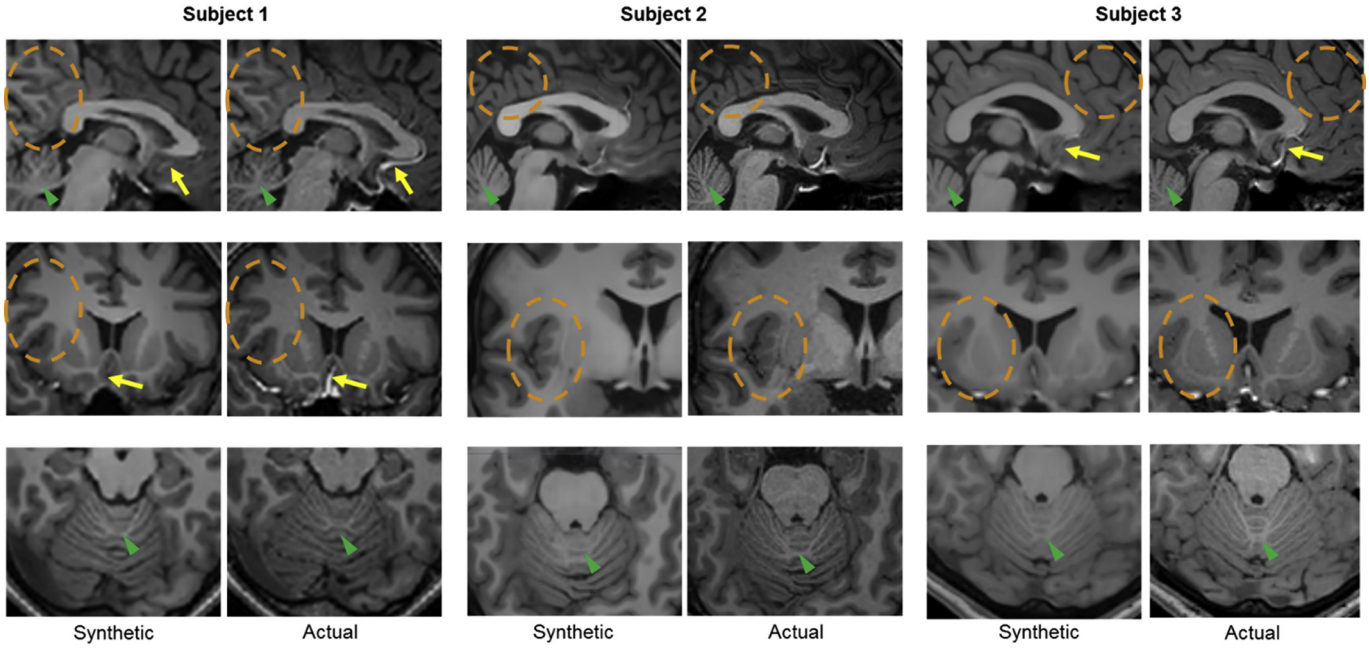

Fig. 3. Magnified view from three different subjects in the test set. For each subject, synthetic MPRAGE images for sagittal, coronal, axial views and corresponding actual MPRAGE images are shown.

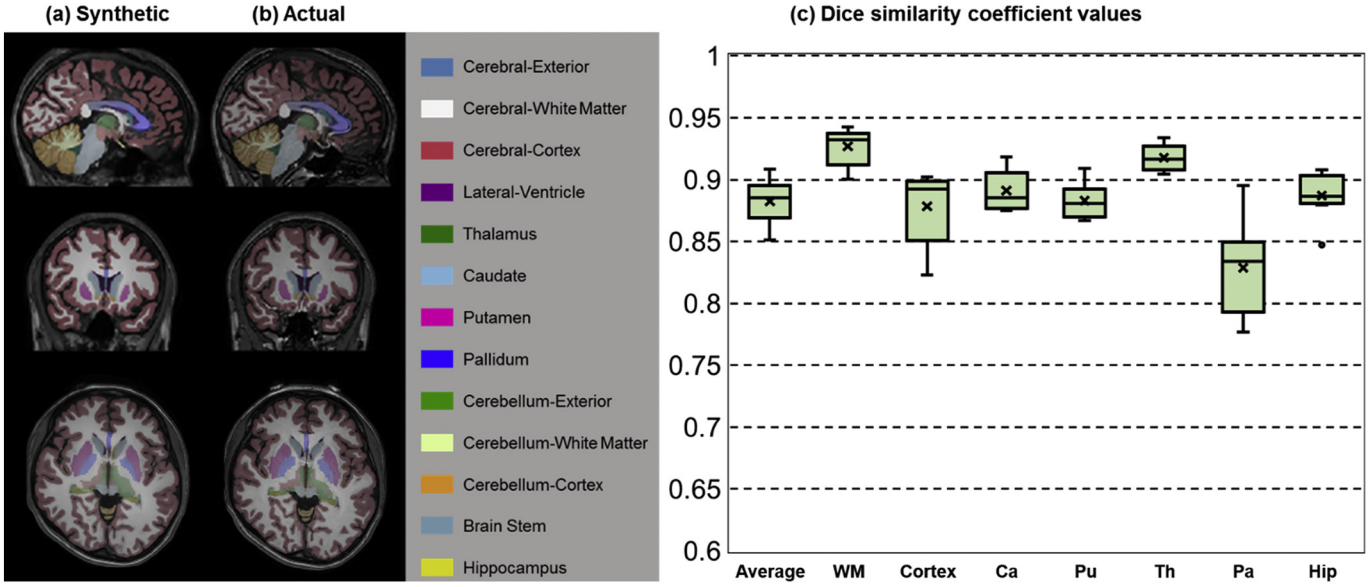

Fig. 4. Segmentation results with actual MPRAGE versus synthetic MPRAGE. Representative segmentation results are overlaid on (a) synthetic MPRAGE and (b) actual MPRAGE images. (c) The box plot of the DSCs of various regions, i.e. total average DSC, cerebral white matter (WM), cortex, caudate (Ca), putamen (Pu), thalamus (Th), pallidum (Pa) and hippocampus (Hip).

pairwise student's *t*-test (two-tailed test) was performed and a *p*-value of 0.05 or smaller was considered statistically significant. Moreover, correlation analyses were performed between the two measurements.

Lastly, to investigate how the proposed method performs on unfamiliar datasets, clinical data with pathologic lesions were obtained and tested. Note that the training was processed only on the data of healthy volunteers. The synthetic MPRAGE images were generated from the mGRE images of clinical database. The performance was visually evaluated by a radiologist focusing on the pathologic lesions.

3. Results

Fig. 2 illustrates mGRE images for each four echo times, the synthetic MPRAGE and the actual MPRAGE for one subject in the test set. Compared with the input mGRE images, the synthetic MPRAGE images show superior delineation of white matter and gray matter contrasts in both cortical and subcortical regions. Overall, the synthetic and actual MPRAGE show similar contrasts for most regions. Although the reconstructed synthetic data is from patched data which are fragments of the entire 3D image, using the overlap-tile scheme resulted in a natural reconstruction without discontinuities which turned out to be an important requisite for the study (results not shown).

Fig. 3 shows magnified views of the synthetic and actual MPRAGE images from three different subjects in the test set. Slices from similar locations were selected and three orthogonal plane images are shown. Here, it can be observed that the results are consistent for different

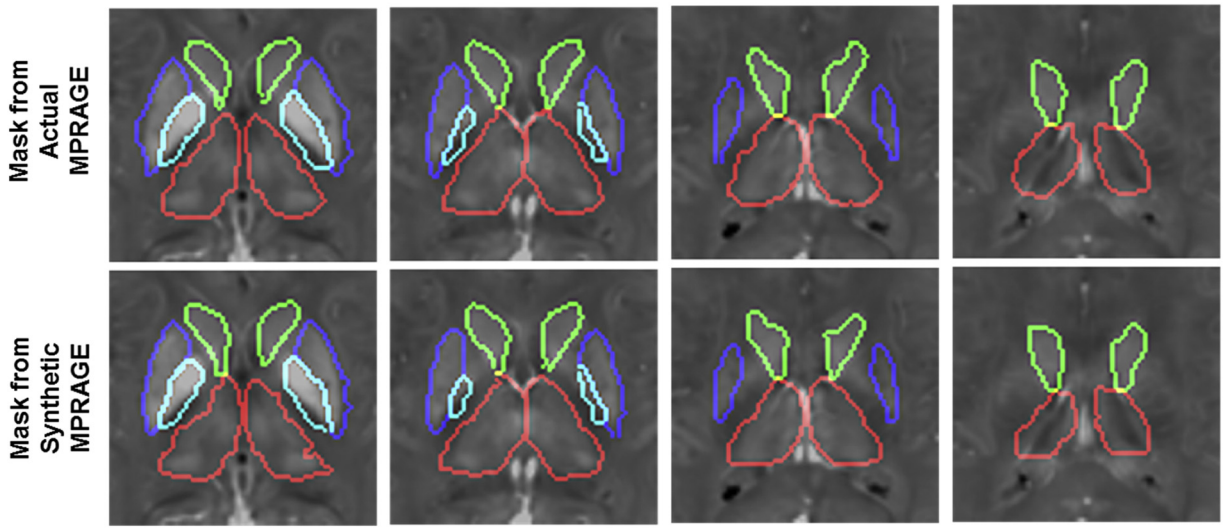

Fig. 5. Representative susceptibility images with overlaid ROIs from actual MPRAGE (top) and synthetic MPRAGE (bottom) for subcortical structures of interests, i.e. caudate (green), putamen (blue), pallidum (light blue), thalamus (red). (For interpretation of the references to colour in this figure legend, the reader is referred to the web version of this article.)

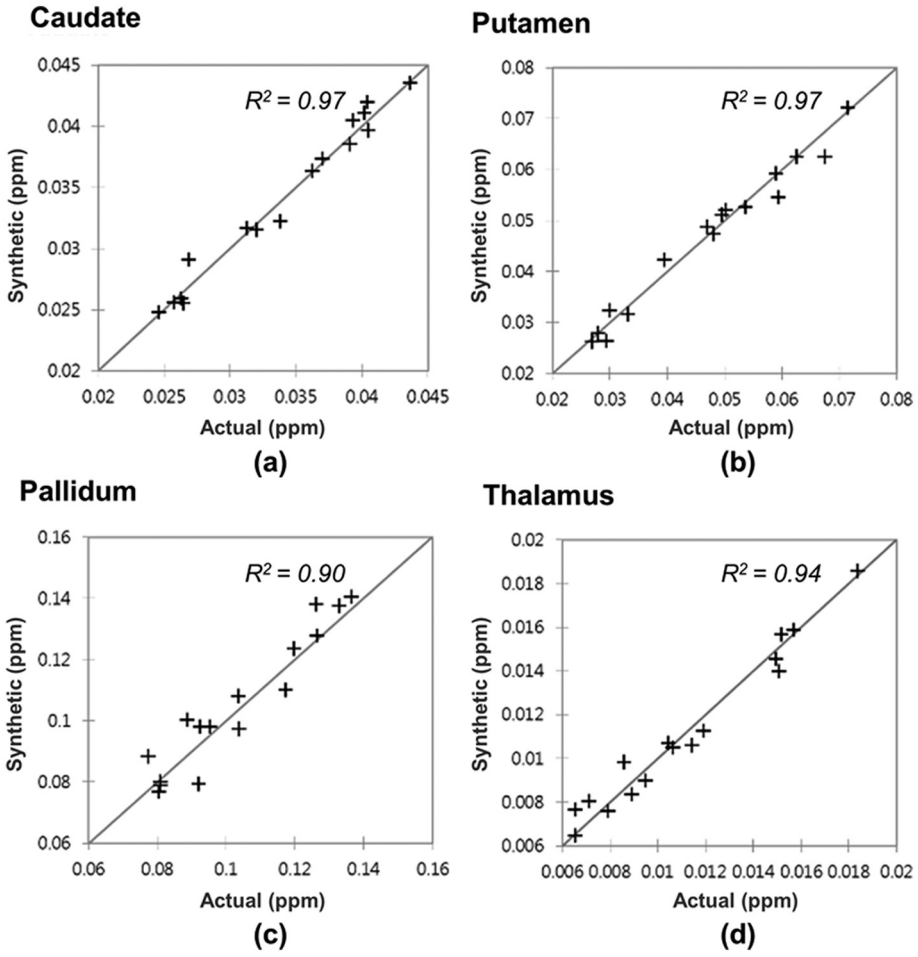

Fig. 6. (a, b, c, d) Scatter plot for mean tissue susceptibility estimates between the two ROIs (Actual MPRAGE, Synthetic MPRAGE). The correlation coefficients between the two susceptibility measurements are high for all regions ($R^2 > 0.9$).

subjects. Specifically, boundaries of the cortical structures (orange dashed circles) which were difficult to delineate in the input mGRE images are well depicted in the synthetic image. Cerebellar (green arrowheads) wrinkles which are particularly difficult to delineate in the mGRE images due to their fine structures have a slight blur, but the overall contour are visible in the synthetic images. Interestingly, high intensity inflow signals that can be observed in both the actual MPRAGE and the 1st and 2nd echoes of mGRE (shown in Fig. 2a) are

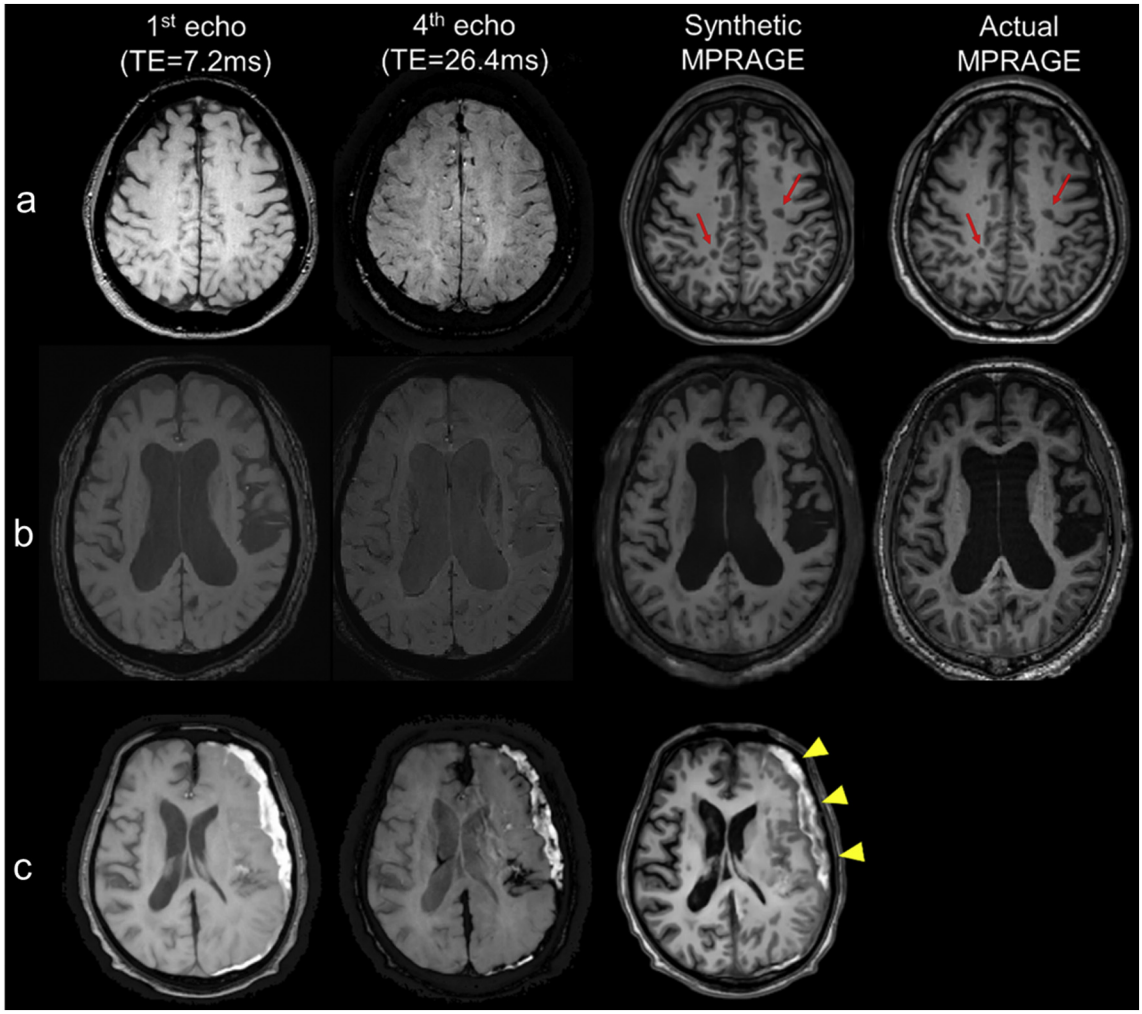

Fig. 7. Results from two patients. (a) A patient with white matter hypointensities (red arrow), (b) a patient with brain atrophy, and (c) a patient with late subacute subdural hemorrhage in the left cerebral convexity (yellow arrowhead). The mGRE data of the first and last TE, synthetic MPRAGE, and actual MPRAGE are shown. For the third patient (c), the actual MPRAGE was not obtained for this patient. (For interpretation of the references to colour in this figure legend, the reader is referred to the web version of this article.)

mostly suppressed in the synthetic MPRAGE images (yellow arrows). The average NRMSE and SSIM values for all subjects in test set were 0.037 ± 0.009 and 0.84 ± 0.03, respectively, which show the image similarity of the synthetic MPRAGE compared to the conventional.

Fig. 4 shows the segmentation results from the synthetic MPRAGE (Fig. 4a) and actual MPRAGE (Fig. 4b). The automatically segmented tissue regions are overlaid onto the synthetic and the actual MPRAGEs. Fig. 4(c) shows the box plot of the calculated DSC values for different regions computed from all subjects in the test set. The calculated DSCs were 0.93 ± 0.02, 0.88 ± 0.03, 0.89 ± 0.02, 0.88 ± 0.01, 0.92 ± 0.01, 0.83 ± 0.04, 0.89 ± 0.02 for cerebral white matter, cortex, caudate, putamen, thalamus, pallidum and hippocampus, respectively. The average DSC was 0.88 ± 0.02. For these regions, the DSCs showed high consistencies between the two results and were in the range of 0.82 to 0.95 for all the subjects.

Fig. 5 shows representative QSM images with overlaid deep gray matter regions using segmentation from the actual MPRAGE and synthetic MPRAGE. The individual ROIs obtained for both methods show similar delineations for the deep gray matter regions. Fig. 6 shows the scatter plot for the mean tissue susceptibility estimates from the regions obtained between the two methods. Both measurements are in good agreement and no distinct outlier could be observed in the scatter plot. There were no statistically significant differences between the two methods ($p > 0.05$ for all regions). The correlation coefficients between the two susceptibility measurements were high for all regions ($R^2 = 0.97, 0.97, 0.90$, and 0.94 for caudate, putamen, pallidum, and thalamus, respectively).

Fig. 7 shows the tested clinical images obtained with known pathologies. The first subject (Fig. 7a) had several abnormal white matter hypointense lesions (red arrows). The second subject (Fig. 7b) had brain atrophy. The descriptions of these lesions are consistent on the synthetic and actual MPRAGEs. The third subject (Fig. 7c) had a subdural hemorrhage (yellow arrowheads). Although the actual MPRAGE was not acquired for this patient, the synthetic MPRAGE depicts well the large hemorrhagic lesion without unnatural contrasts that often occur in overfitting models. The representative results for other clinical patient data are shown in the supplementary material.

4. Discussion and conclusion

In this work, we applied a deep learning method for synthetic MPRAGE generation using mGRE images. The method utilizes a 3D fully convolutional neural network for synthesizing the MPRAGE from the mGREs. Overall, the network demonstrated to produce synthetic MPRAGE images which were close to the actual MPRAGE for the major brain tissues. By visual inspection, the contrast between the white matter and the gray matter regions looks comparable to that of the actual MPRAGE. Quantitative evaluation based on automatic tissue

segmentation also shows a high agreement between the results from the two MPRAGE images, demonstrating the practical utility of synthetic MPRAGE. Moreover, using the segmentation outputs, we have demonstrated that there is no statistically significant difference between the mean susceptibility values of the QSMs obtained with ROIs from synthetic MPRAGE and from actual MPRAGE.

While the overall image quality of the synthetic MPRAGE was close to that of the actual MPRAGE, there were some minor differences between the actual and synthetic MPRAGE images. Even though we used additional TV loss to alleviate image blurring, slight blur remains especially near the boundary regions with an indistinct contrast between tissues. These are suspected to be due to the drawbacks of using the Euclidean metrics for the loss function which has been reported to cause over-smoothing effect under inherent uncertainty [30]. In addition, the inflow signals were not consistent in synthetic and actual MPRAGE images. Most bright inflow signals appearing in the actual MPRAGE images were suppressed in the synthetic images. This is suspected to be due to the inconsistency of the inflow signals between different echo time images of mGRE due to incomplete flow compensations. Specifically, in the first echo images (which are strongly flow compensated) the inflow bright signals are consistent with the MPRAGE signal intensities but in other echo images (which are partially flow compensated) the intensities are not consistent. Nevertheless, we believe these two minor differences are not a problem for using synthetic MPRAGE for registration or segmentation purposes.

Compared to other regions, the DSC was slightly lower in the pallidum region, and there was a relatively higher difference in the susceptibility measurement. To resolve this, it would be useful to acquire more dataset for the training or replace the MPRAGE with other variations of this sequence such as MP2RAGE that have been reported to have a better delineation of this region [31]. Furthermore, it might have been due to the inherent error of the automatic segmentation algorithm. The segmentation of pallidum was reported to be challenging and significantly less accurate than other structures likely due to the small size [32].

The outcome of the two subjects with pathologies is encouraging to support the network's generalization performance to unseen dataset. Though the network was trained with subjects of the specific group (Healthy subjects of ages: 25–30), the synthesized images for the subjects (age > 50) with pathologies seemed qualitatively acceptable. However, further exploration with additional datasets of various subject groups will be needed to understand the capability of the network to generalize. Moreover, in this study the network has been tested only on restricted acquisition parameters such as voxel size, TR, TE etc. For general utilization of this method, performance on varying acquisition parameter should be tested.

Since the network was trained only by data and without specific guidance, it is difficult to understand and interpret the outcomes. Recently, a study suggested an interpretation that success of deep learning methods stems from utilizing a nonlocal basis combined with a data-driven local basis [33]. As mGRE produces multi echo images, it possesses variety of information of the tissue dependent T_2* and T_1 contrasts. A combination of these multi-echo images has shown capability of generating a plural of contrast images [34]. We speculate that this variety of information might have been complementarily incorporated to synthesize a highly reliable MPRAGE image.

There are mainly two benefits of synthetizing MPRAGE images. First, this method can be applicable when acquiring MPRAGE is difficult (i.e. tight scheduled protocols) or when MPRAGE has not been acquired. Second additional benefit is that synthetic MPRAGE is automatically registered to the mGRE images, as the synthetic MPRAGE is generated from them. This may be beneficial for decreasing registration error, and may also save time and effort for registration. In summary, the current study suggests that deep learning can potentially be used to synthesize MPRAGE from mGRE, which can provide potential values for reducing scan time and improve analysis tasks.

Acknowledgments

This research was supported by Basic Science Research Program through the National Research Foundation of Korea (NRF) funded by the Ministry of Science, ICT and Future Planning (NRF-2017R1D1A1B03030772, NRF-2018M3C7A1056884, NRF-2016R1C1B1009247).

The research was supported by Graduate Student Scholarship Program funded by Hyundai Motor Chung Mong-Koo Foundation.

References

[1] Mugler John P, Brookeman James R. Three-dimensional magnetization-prepared rapid gradient-echo imaging (3D MP RAGE). Magn Reson Med 1990;15(1):152–7.
[2] Yao B, Li T-Q, Pv Gelderen, Shmueli K, de Zwart JA, Duyn JH. Susceptibility contrast in high field MRI of human brain as a function of tissue iron content. NeuroImage 2009;44(4):1259–66.
[3] Cohen-Adad J. What can we learn from T2* maps of the cortex? NeuroImage 2014;93:189–200.
[4] Langkammer C, Schweser F, Krebs N, Deistung A, Goessler W, Scheurer E, et al. Quantitative susceptibility mapping (QSM) as a means to measure brain iron? A post mortem validation study. NeuroImage 2012;62(3):1593–9.
[5] Langkammer C, Liu T, Khalil M, Enzinger C, Jehna M, Fuchs S, et al. Quantitative susceptibility mapping in multiple sclerosis. Radiology 2013;267(2):551–9.
[6] Betts MJ, Acosta-Cabronero J, Cardenas-Blanco A, Nestor PJ, Duzel E. High-resolution characterisation of the aging brain using simultaneous quantitative susceptibility mapping (QSM) and R2* measurements at 7T. Neuroimage 2016;138(Supplement C):43–63.
[7] Hagemeier J, Zivadinov R, Dwyer MG, Polak P, Bergsland N, Weinstock-Guttman B, et al. Changes of deep gray matter magnetic susceptibility over 2 years in multiple sclerosis and healthy control brain. NeuroImage: Clinical 2017.
[8] Acosta-Cabronero J, Betts MJ, Cardenas-Blanco A, Yang S, Nestor PJ. In vivo MRI mapping of brain Iron deposition across the adult lifespan. J Neurosci 2016;36(2):364–74.
[9] Polak D, Setsompop K, Cauley Stephen F, Gagoski Borjan A, Bhat H, Maier F, et al. Wave-CAIPI for highly accelerated MP-RAGE imaging. Magn Reson Med 2017;79(1):401–6.
[10] Liu F, Jang H, Kijowski R, Bradshaw T, McMillan AB. Deep learning MR imaging-based attenuation correction for PET/MR imaging. Radiology 2018;286(2):676–84.
[11] Han X. MR-based synthetic CT generation using a deep convolutional neural network method. Med Phys 2017;44(4):1408–19.
[12] Xiang L, Wang Q, Nie D, Zhang L, Jin X, Qiao Y, et al. Deep embedding convolutional neural network for synthesizing CT image from T1-weighted MR image. Med Image Anal 2018;47:31–44.
[13] Bahrami K, Rekik I, Shi F, Shen D. Joint reconstruction and segmentation of 7T-like MR images from 3T MRI based on cascaded convolutional neural networks. Medical image computing and computer-assisted intervention: MICCAI international conference on medical image computing and computer-assisted intervention. vol. 10433. 2017. p. 764–72.
[14] Chartsias A, Joyce T, Giuffrida MV, Tsaftaris SA. Multimodal MR synthesis via modality-invariant latent representation. IEEE Trans Med Imaging 2018;37(3):803–14.
[15] Roy S, Jog A, Carass A, Prince JL. Atlas based intensity transformation of brain MR images. In: Shen L, Liu T, Yap P-T, Huang H, Shen D, Westin C-F, editors. Multimodal Brain Image Analysis. Cham: Springer International Publishing; 2013. p. 51–62.
[16] Roy S, Carass A, Prince J. A compressed sensing approach for MR tissue contrast synthesis. In: Székely G, Hahn HK, editors. Information processing in medical imaging. Berlin, Heidelberg: Springer Berlin Heidelberg; 2011. p. 371–83.
[17] Jenkinson M, Beckmann CF, Behrens TEJ, Woolrich MW, Smith SM. FSL. NeuroImage 2012;62(2):782–90.
[18] Olaf Ronneberger PF, Brox Thomas. U-Net: Convolutional networks for biomedical image segmentation. arXiv:150504597; 2015.
[19] Han X. MR-based synthetic CT generation using a deep convolutional neural network method. Med Phys 2017;44(4):1408–19.
[20] Lee D, Yoo J, Ye JC. Deep residual learning for compressed sensing MRI. 2017 IEEE 14th international symposium on biomedical imaging (ISBI 2017). 2017. p. 15–8.
[21] Özgün Çiçek AA, Lienkamp Soeren S, Brox Thomas, Ronneberger Olaf. 3D U-Net: learning dense volumetric segmentation from sparse annotation. arXiv 2016;160606650.
[22] Johnson J, Alahi A, Fei-Fei L. Perceptual losses for real-time style transfer and super-resolution. In: Leibe B, Matas J, Sebe N, Welling M, editors. Computer vision – ECCV 2016. Cham: Springer International Publishing; 2016. p. 694–711.
[23] Yoon J, Gong E, Chatnuntawech I, Bilgic B, Lee J, Jung W, et al. Quantitative susceptibility mapping using deep neural network: QSMnet. Neuroimage 2018;179:199–206.
[24] Mathieu M, Couprie C, LeCun. Deep multi-scale video prediction beyond mean square error. 2015. [arXiv preprint arXiv:.05440].
[25] Wang Z, Bovik AC, Sheikh HR, Simoncelli EP. Image quality assessment: from error visibility to structural similarity. IEEE Trans Image Process 2004;13:600–12.
[26] Reuter M, Schmansky NJ, Rosas HD, Fischl B. Within-subject template estimation for unbiased longitudinal image analysis. NeuroImage 2012;61(4):1402–18.

[27] Zou KH, Warfield SK, Bharatha A, Tempany CMC, Kaus MR, Haker SJ, et al. Statistical validation of image segmentation quality based on a spatial overlap index[1]. Acad Radiol 2004;11(2):178–89.
[28] Schweser F, Deistung A, Lehr BW, Reichenbach JR. Quantitative imaging of intrinsic magnetic tissue properties using MRI signal phase: an approach to in vivo brain iron metabolism? NeuroImage 2011;54(4):2789–807.
[29] Li W, Wang N, Yu F, Han H, Cao W, Romero R, et al. A method for estimating and removing streaking artifacts in quantitative susceptibility mapping. NeuroImage 2015;108:111–22.
[30] Isola P, Zhu J-Y, Zhou T, Efros AA. Image-to-image translation with conditional adversarial networks.
[31] Okubo G, Okada T, Yamamoto A, Kanagaki M, Fushimi Y, Okada T, et al. MP2RAGE for deep gray matter measurement of the brain: a comparative study with MPRAGE. J Magn Reson Imaging 2015;43(1):55–62.
[32] Dolz J, Desrosiers C, Ben Ayed I. 3D fully convolutional networks for subcortical segmentation in MRI: a large-scale study. NeuroImage 2018;170:456–70.
[33] Ye JC, Han Y, Cha E. Deep convolutional framelets: a general deep learning framework for inverse problems. Siam Journal on Imaging Sciences 2018;11(2):991–1048.
[34] Luo J, Jagadeesan BD, Cross AH, Yablonskiy DA. Gradient echo plural contrast imaging — signal model and derived contrasts: T2*, T1, phase, SWI, T1f, FST2*and T2*-SWI. NeuroImage 2012;60(2):1073–82.